

## Supporting Information

### (De)Sodiation via Helical Phosphorus Intermediates in High Capacity Anodes for Sodium-ion Batteries

Lauren E. Marbella,<sup>a</sup> Matthew L. Evans,<sup>b</sup> Matthias F. Groh,<sup>a</sup> Joseph Nelson,<sup>b</sup> Kent J. Griffith,<sup>a</sup> Andrew J. Morris,<sup>c,\*</sup> and Clare P. Grey<sup>a,\*</sup>

<sup>a</sup>Department of Chemistry, University of Cambridge, Lensfield Road, Cambridge CB2 1EW, United Kingdom

<sup>b</sup>Theory of Condensed Matter Group, Cavendish Laboratory, University of Cambridge, J. J. Thomson Avenue, Cambridge CB3 0HE, United Kingdom

<sup>c</sup>School of Metallurgy and Materials, University of Birmingham, Edgbaston, Birmingham B15 2TT, United Kingdom

#### Table of Contents

Electrochemistry. ....	2
Solid-state NMR spectroscopy.....	5
Note on P motifs in structural models that resemble experimental data. ....	10
Powder X-ray diffraction. ....	13
References.....	18

### Electrochemistry.

By using 1.0 M NaFSI in 2-MeTHF as the electrolyte, the  $\text{Na}_x\text{P}$  batteries exhibit one of the highest reversible capacities in the first cycle of  $2074 \pm 80 \text{ mA h g}^{-1}$  without the use of electrolyte additives to date. Unfortunately, over the course of multiple cycles, the Na-ion batteries (NIBs) exhibit poor capacity retention, with only 68% of the original capacity achieved in the 10th cycle (Figure S1). The corresponding  $dQ/dV$  curves for the electrochemistry of the first cycle are shown in Figure S2.

High first cycle capacities were observed provided the rate was kept below C/20 (Figure S3). Performance begins to decline at a rate of C/5 (Figure S3) and the black P NIBs fail to provide high capacity at C-rates faster than 1C (Figure S4). Electrochemical cycling tests on films comprised of only the carbon mixture indicate that carbon contributes minimally to the observed capacity (Figure S5); thus, reported capacities were calculated based on the weight of phosphorus alone.

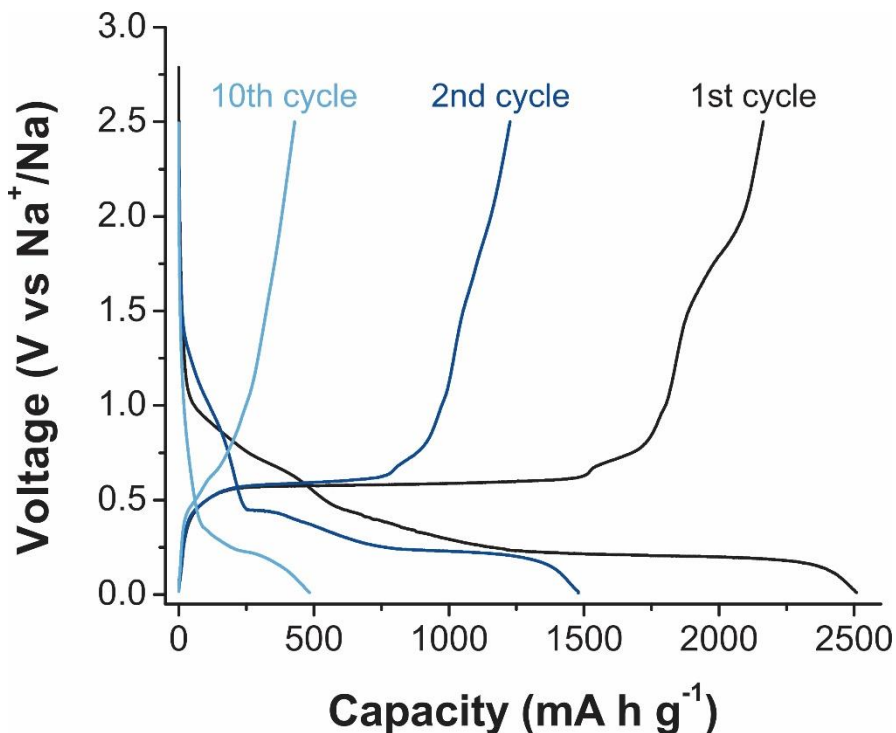


**Figure S1.** Discharge/charge (sodiation/desodiation) curves for the 1<sup>st</sup>, 2<sup>nd</sup>, and 10<sup>th</sup> cycles of black P electrodes.

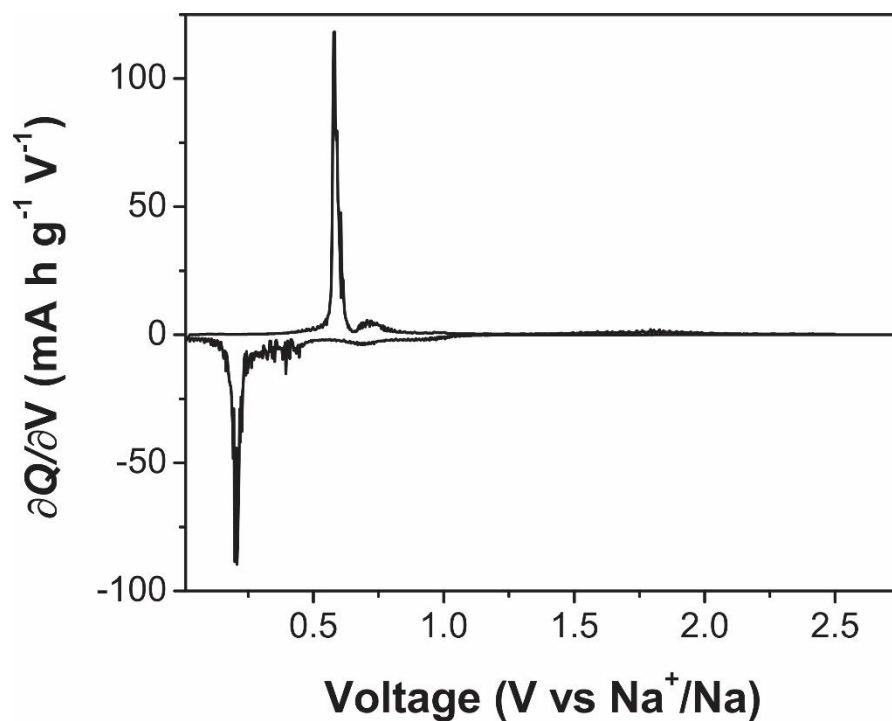


**Figure S2.** Corresponding  $dQ/dV$  curves for electrochemical data (1<sup>st</sup> cycle) shown in Figure S1 of the main text (C/100).

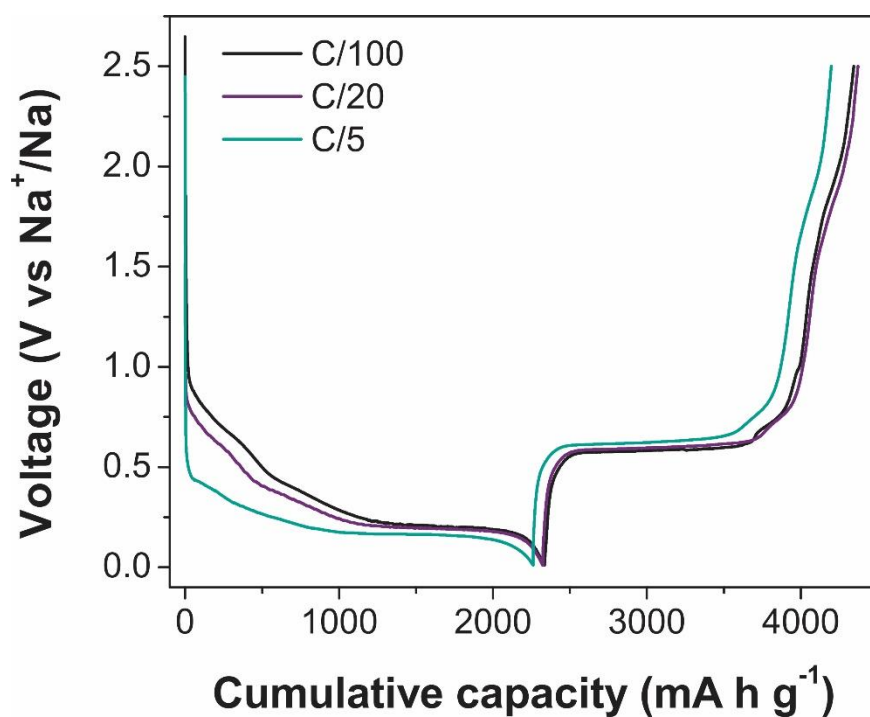


**Figure S3.** Electrochemistry of black P electrodes over one full discharge-charge cycle at C/100 (black), C/20 (purple), and C/5 (teal).

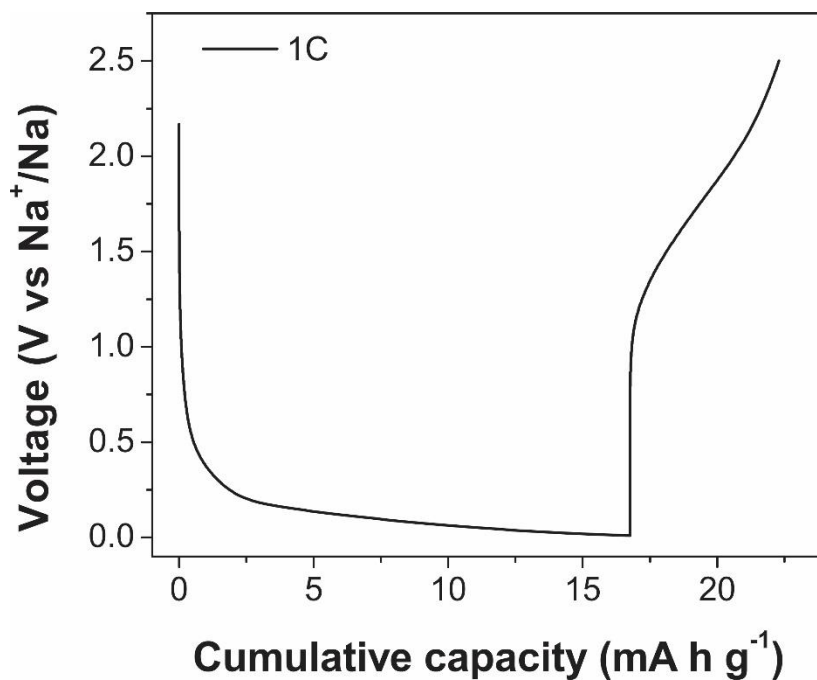


**Figure S4.** Electrochemistry of black P electrodes over one full discharge-charge cycle at 1C.

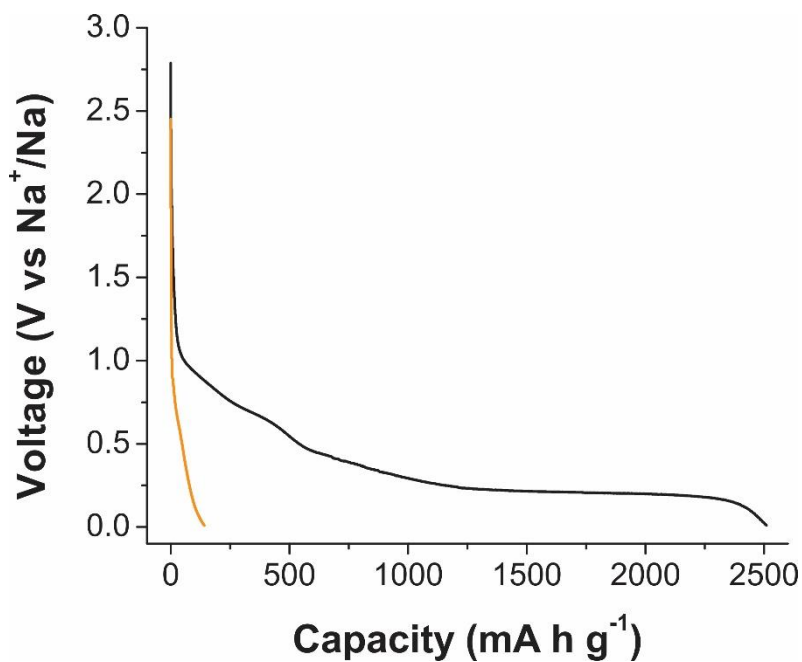


**Figure S5.** Discharge (sodiation) profile for black P electrodes with P:C = 50:50 (black) compared to the carbon mixture only (orange).

### Solid-state NMR spectroscopy.

Two different field strengths were used to measure  $^{23}\text{Na}$  NMR (Figure 4 and Figure S6) because the second order quadrupole interaction ( $^{23}\text{Na}$   $I = 3/2$ ) is only partially averaged by MAS, yet is inversely proportional to the applied field strength. Spectra recorded at lower fields exhibit more dramatic second-order quadrupolar broadening, whereas spectra obtained at higher fields provide higher resolution<sup>1</sup>. Acquiring measurements at multiple fields provides a sensitive probe of local  $^{23}\text{Na}$  environments because information on the quadrupolar coupling and chemical shift tensors can be assessed and compared to theory, providing spectral fingerprints for different  $\text{Na}_x\text{P}$  phases that are more difficult to evaluate in the  $^{31}\text{P}$  NMR ( $^{31}\text{P}$   $I = 1/2$ ) spectra. For instance, both structure models of  $c\text{-Na}_3\text{P}$  ( $P6_3/mmc$  and  $P6_3cm$ ) feature only one independent P position. DFT calculations of the corresponding  $^{31}\text{P}$  shifts appear in similar spectral regions ( $-180$  vs  $-217$  ppm for  $P6_3cm$  vs  $P6_3/mmc$ , respectively) and fall on either side of the experimentally observed value ( $-207$  ppm). Conversely, variable field  $^{23}\text{Na}$  NMR showed distinct differences for these two structural models.

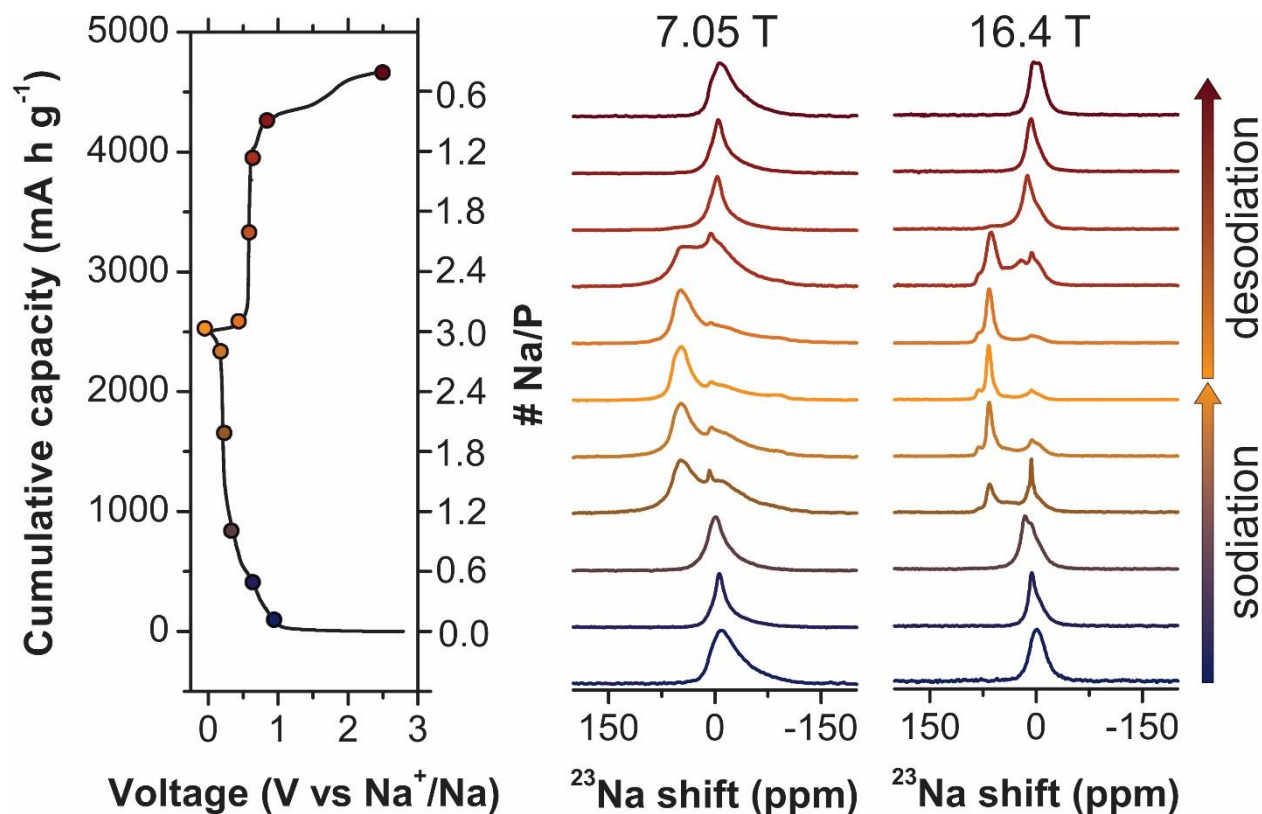


**Figure S6.** *Ex situ*  $^{23}\text{Na}$  MAS NMR spectra (MAS = 60 kHz) of black P recorded at various stages of sodiation/desodiation at 7.05 T (middle) and 16.4 T (right) with the corresponding electrochemistry (left). The circles on the electrochemical profile indicate the points where cycling was arrested and samples were extracted for the NMR experiments.

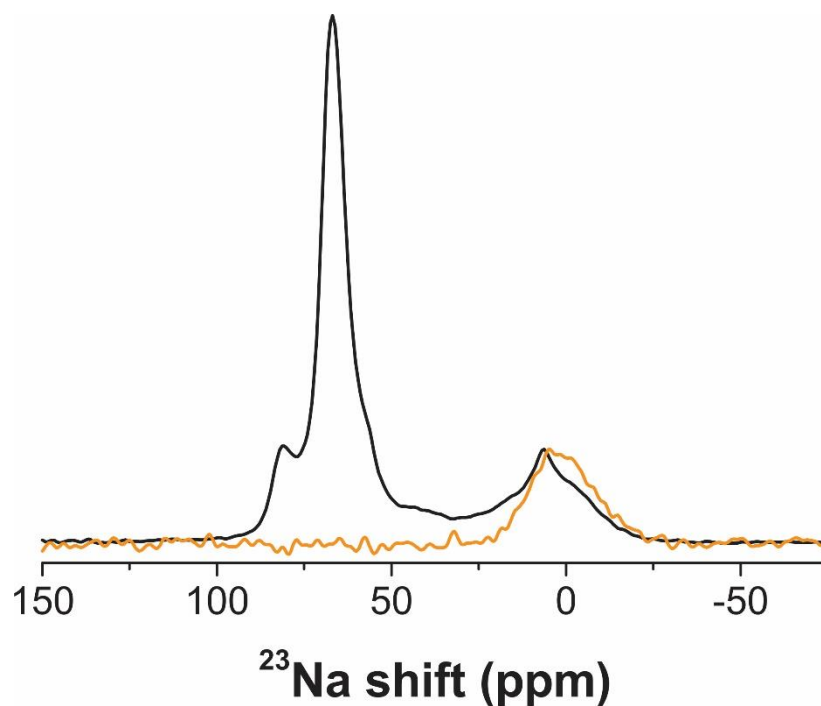


**Figure S7.** Overlay of  $^{23}\text{Na}$  MAS NMR of  $\text{Na}_x\text{P}$  electrodes at the end of sodiation (0.01 V, black) compared to carbon only electrodes discharged to 0.01 V (orange) at 16.4 T.

Slight deviations between the  $^{31}\text{P}$  MAS spectra acquired at 60 kHz (Figure 2b) and the isotropic projections shown in Figures 4 and S9 are likely due to selective spin-spin relaxation ( $T_2$ )-weighting in the  $^{31}\text{P}$  PASS experiment from the application of the five consecutive  $\pi$  pulses.

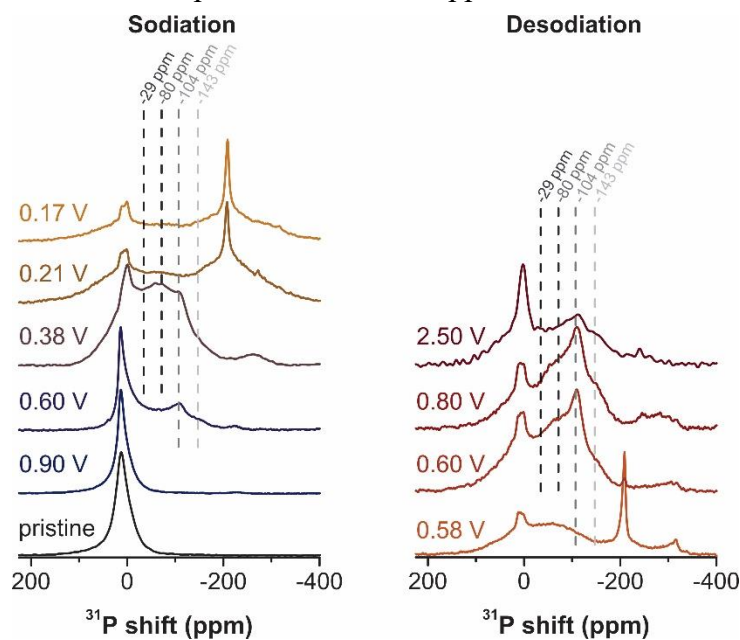


**Figure S8.** Magnified *ex situ*  $^{31}\text{P}$  MAS NMR spectra during the initial and final stages of sodiation/desodiation, respectively.

The amorphous NaP species formed on (de)sodiation exhibit rapid  $T_2$  ( $<1$  ms), some of which may be completely dephased by the end of the rotor period (100  $\mu$ s), resulting in an emphasis of certain resonances over others in the 2D  $^{31}\text{P}$  PASS analysis. While our analysis suggests the formation of P helices and P zig-zags, other morphologies and sites within these motifs with extremely short  $T_2$  values may suffer from poor signal-to-noise in PASS and not be analyzed.

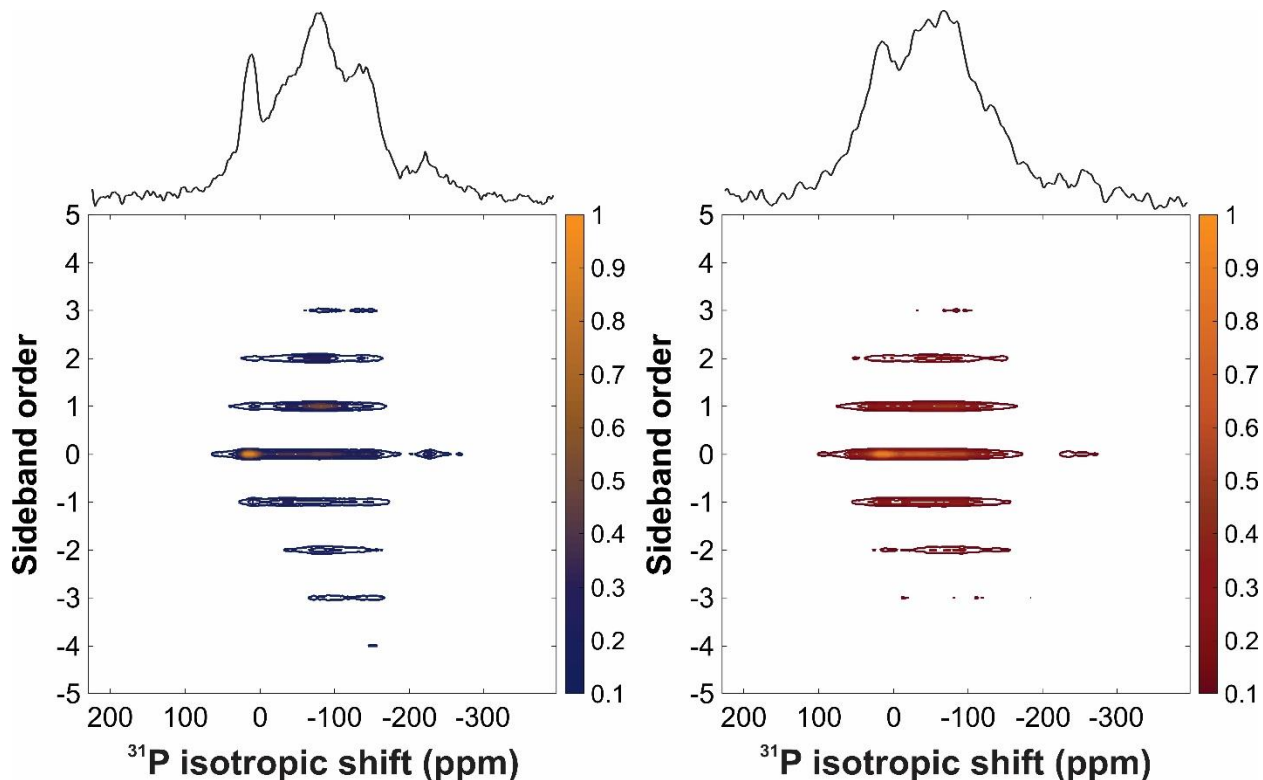


**Figure S9.** 2D  $^{31}\text{P}$  PASS spectra acquired at MAS = 10 kHz of NIBs at 0.38 V (780 mA h  $\text{g}^{-1}$ ) during sodiation (left) and 0.80 V (4240 mA h  $\text{g}^{-1}$ ) during desodiation, which both correspond to Na:P stoichiometries of approximately 1:1.

Despite the fact that the experimental sideband pattern for  $\delta_{\text{iso}} = -143$  ppm was not well described by a CSA pattern (Figure S10), similar CS tensor parameters were obtained at both 10 and 12 kHz MAS. The CSA pattern that most closely corresponds to that of the simulated fit belongs to P2 in metastable  $\text{Na}_7\text{P}_8$  (+54.824 meV above the hull). The extended P structure in this model consists of P helices and does not alter the interpretation of the P motifs present in *a*-NaP during desodiation.

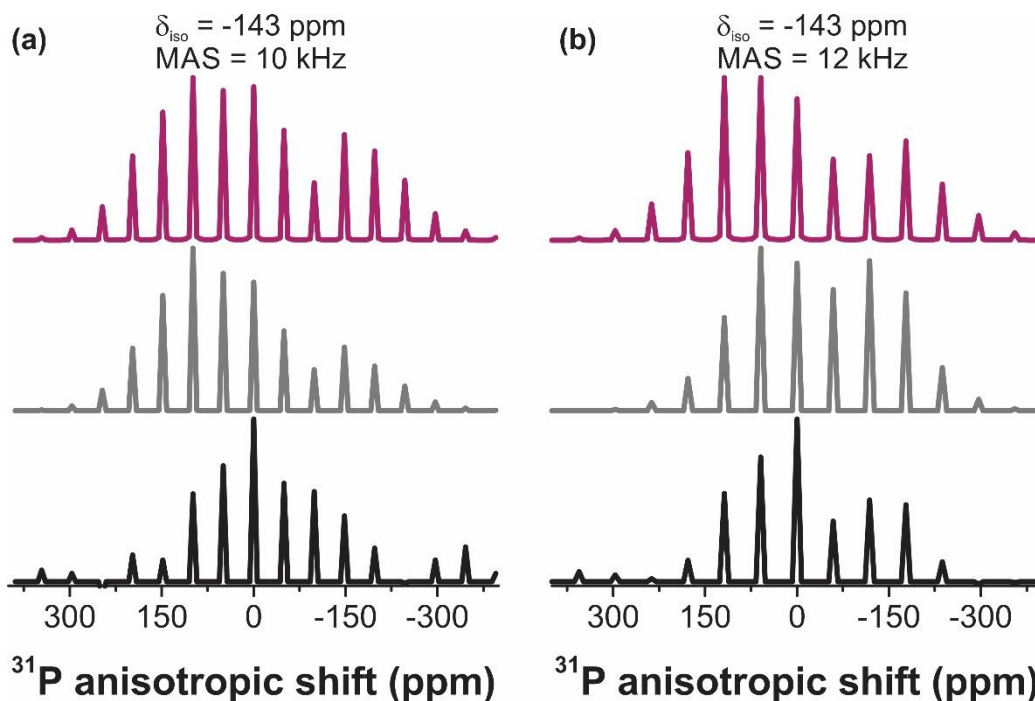


**Figure S10.** Experimental anisotropic projections from 2D  $^{31}\text{P}$  PASS experiments showing sideband patterns (bottom, black) for  $\delta_{\text{iso}} = -143$  ppm obtained at 0.80 V during desodiation at 10 (a) and 12 kHz (b) MAS speed. Simulated patterns (middle grey) show CSA tensor parameters of  $\Delta = -459$  ppm and  $\eta = 0.61$  for (a) and  $\Delta = -402$  ppm and  $\eta = 0.63$  for (b). The calculated sideband pattern for P2 in metastable  $\text{Na}_7\text{P}_8$  (+55 meV above the hull, top, purple) is shown for comparison.

The anisotropic projections corresponding to the resonances at 14 and  $-235$  ppm show small anisotropies (Figure S11), hindering the information that can be gained from analysis of the CSA at these positions because the CSA tensors cannot be reliably fit due to the limited number and intensity of sidebands. The  $^{31}\text{P}$  resonance at 14 ppm is assigned to black P because a single crystallographic environment with small anisotropy is expected and the isotropic shift coincides with that of the pristine material.

It is worth noting that solid-state NMR experiments that separate isotropic and anisotropic chemical shift interactions, such as magic-angle turning (MAT),<sup>2</sup> PASS,<sup>3-4</sup> and combined MATPASS have been successfully used to assign structural motifs in a variety of amorphous materials<sup>5-10</sup>. While several variations of 2D MATPASS have been used to probe multiple nuclei in battery materials as a function of composition and state of charge<sup>5-10</sup>, PASS experiments have not been employed, likely due to the prevalence of paramagnetism in electrode materials. Paramagnetic materials often exhibit extremely broad lineshapes, often covering a bandwidth that the train of five  $\pi$  pulses in conventional PASS sequences cannot effectively excite. Further, in the MATPASS experiments that have been carried out, an emphasis has largely been placed on analyzing isotropic projections, which provide high resolution “infinite spinning speed” spectra. With the large hyperfine shift range typically observed in paramagnetic materials, the isotropic chemical shift alone is often a reliable spectral fingerprint of the chemical structure. Yet, in all of these experiments, each isotropic slice is correlated to an anisotropic spectrum that provides information on the electron density around the nuclei that is related to the geometry of the chemical bonding environments and structures of molecular fragments<sup>11</sup>. Analysis of the full chemical shift tensor is necessary to correlate the CSA with specific coordination environments and as such, is

significantly more rigorous than analysis of the isotropic shift alone, where both experiment and theory are susceptible to fortuitous overlap and/or cancellation of errors.

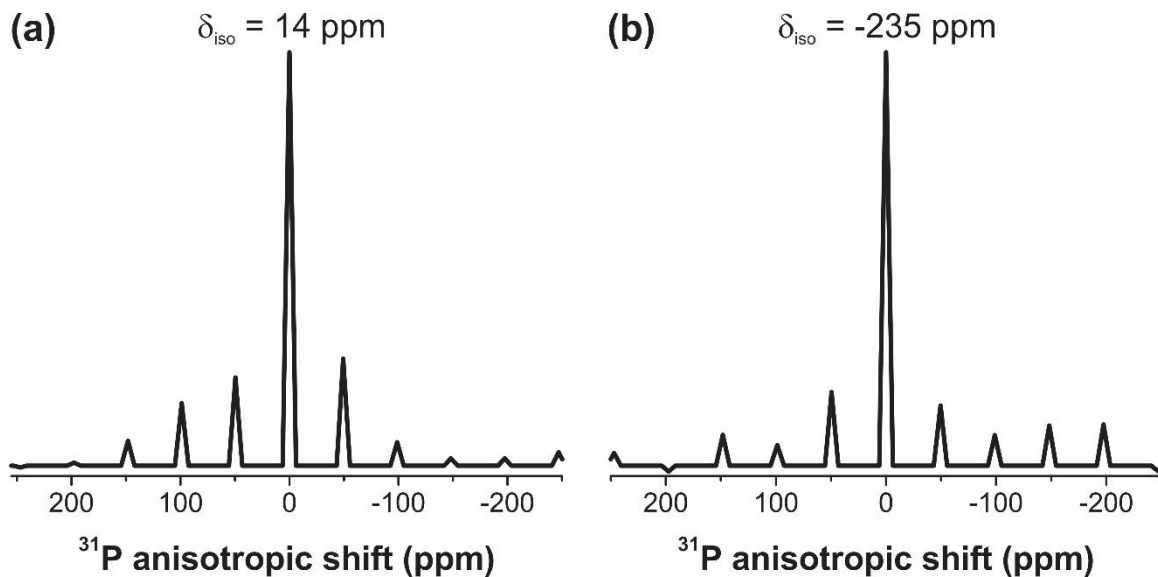


**Figure S11.** Experimental anisotropic projections from 2D  $^{31}\text{P}$  PASS experiments at MAS = 10 kHz of NIBs at 0.38 V ( $780 \text{ mA h g}^{-1}$ ) showing sideband patterns for (a)  $\delta_{\text{iso}} = 14$  ppm and (b)  $\delta_{\text{iso}} = -235$  ppm.

**Table S1.** Experimental  $^{31}\text{P}$  CS tensors obtained for NIBs at 0.38 V (780 mA h g $^{-1}$ ) during sodiation and 0.80 V (4240 mA h g $^{-1}$ ) during desodiation and calculated CS tensor parameters for individual  $^{31}\text{P}$  sites in structural models with stoichiometries at or near NaP. The best match from the main text is shown immediately below the given site.

$^{31}\text{P}$ site/compound	$\delta_{\text{iso}}$ (ppm)	$\Delta$ (ppm)	$\eta$	description
Experimental (780 mA h g $^{-1}$ )	-29	179	0.72	n/a
P2 NaP +96 meV above hull <sup>[a]</sup>	-21	171	0.55	P helix
P1 Na <sub>2</sub> P +95 meV above hull <sup>[b]</sup>	-246	156	0.68	P dumbbells
Experimental (780 mA h g $^{-1}$ )	-78	-261	0.75	n/a
P3 NaP +75 meV above hull <sup>[b]</sup>	-109	-291	0.71	P helix
P4 NaP +75 meV above hull <sup>[b]</sup>	-96	-269	0.85	P helix
P2 NaP +112 meV above hull <sup>[a]</sup>	10 <sup>[c]</sup>	-228	0.68	P helix
P1 Na <sub>2</sub> P +90 meV above hull <sup>[b]</sup>	-33 <sup>[c]</sup>	-240	0.64	P dumbbells
Experimental (780 mA h g $^{-1}$ )	-143	-432	0.87	n/a
P4 NaP +96 meV above hull <sup>[b]</sup>	92 <sup>[c]</sup>	-438	0.85	P zig-zags
P6 NaP +94 meV above hull <sup>[b]</sup>	-100 <sup>[c]</sup>	-478	0.84	5-member P rings
P1 Na <sub>2</sub> P +91 meV above hull <sup>[a]</sup>	-43	-393	0.88	P dumbbells
Experimental (4240 mA h g $^{-1}$ )	-29	-163	0.95	n/a
P8 Na <sub>7</sub> P <sub>8</sub> +33 meV above hull <sup>[b]</sup>	150 <sup>[b]</sup>	-173	0.79	P helix
P1 NaP +91 meV above hull <sup>[b]</sup>	-65 <sup>[c]</sup>	-160	0.59	3-member P zig-zags
P1 Na <sub>5</sub> P <sub>6</sub> +84 meV above hull <sup>[a]</sup>	-119 <sup>[c]</sup>	-138	0.90	P helix
Experimental (4240 mA h g $^{-1}$ )	-78	-197	0.88	n/a
P1 NaP +89 meV above hull <sup>[b]</sup>	-184	-205	0.59	P helix
P1 NaP +113 meV above hull <sup>[a]</sup>	324 <sup>[c]</sup>	-198	0.49	trigonal planar

[a] Model was found using AIRSS [b] Model was found using GA [c] Model does not exhibit a bandgap and the Knight shift contribution to the isotropic shift was not calculated

### Note on P motifs in structural models that resemble experimental data.

The experimental sideband patterns found for the *a*-NaP phases on discharge/charge were compared to the calculated CS tensors for individual  $^{31}\text{P}$  sites in 38 model structures (Figure S12) with stoichiometries at or near Na<sub>1</sub>P<sub>1</sub> (NaP, Na<sub>5</sub>P<sub>6</sub>, Na<sub>5</sub>P<sub>4</sub>, Na<sub>7</sub>P<sub>8</sub>, Na<sub>8</sub>P<sub>7</sub>) to identify possible P motifs in this composition space as well as 15 model structures for Na<sub>2</sub>P to assess the possibility of P–P dumbbell formation (Figure S12). The number of independent  $^{31}\text{P}$  sites for each structure ranged from 1–9. Comparison of closely matched CS tensors are shown in Table S1. The best matches are listed in Tables 2 and 3 in the main text.

For NIBs discharged to 0.38 V (780 mA h g<sup>-1</sup>), the <sup>31</sup>P site at  $\delta_{\text{iso}} = -29$  ppm agrees well with the CS tensor found for P2 in metastable NaP found from AIRSS (+96 meV above the hull, Figure 4b, Table 2 and Table S1). The P2 site in NaP (+96 meV) is surrounded by six Na (average Na–P interatomic distance =  $3.021 \pm 0.019$  Å) and two P atoms (P–P2 bond length = 2.248 Å). A three-fold P helix winds through the Na network and contains a bond angle of P–P2–P = 111.7°. In addition, the CS tensor at the <sup>31</sup>P site  $\delta_{\text{iso}} = -29$  ppm also resembles that of P1 in Na<sub>2</sub>P +95 meV above hull found via GA (Table S1), which contains P–P dumbbells, although less agreement is observed for the isotropic shift and anisotropy. P1 in Na<sub>2</sub>P +95 meV is surrounded by seven Na atoms (average Na–P interatomic distance =  $3.001 \pm 0.120$  Å) and one P atom (P–P2 bond length = 2.401 Å).

The <sup>31</sup>P environment at  $\delta_{\text{iso}} = -78$  ppm agrees with the CS tensor found for P3 in metastable (+75 meV above the hull) NaP found via GA that also contains 3-fold P helices (Figure 4c, Table 2 and Table S1). In this model, P3 is coordinated to five nearby Na atoms (average Na–P interatomic distance =  $3.047 \pm 0.153$  Å) and two P atoms (P–P3–P bond angle = 117.6° and average P–P bond length =  $2.248 \pm 0.014$  Å). In addition, the CS tensor showed similarity to three alternative <sup>31</sup>P site CS tensors found from DFT calculations – two of which also contain P helices and one that exhibits P–P dumbbells. First, the CS tensor also shows similarity to another <sup>31</sup>P site in NaP +75 meV above hull found via GA; P4, although more deviation in the asymmetry parameter is noted. P4 in NaP +75 meV (GA) is also surrounded by five Na atoms (average Na–P interatomic distance =  $3.248 \pm 0.147$  Å) and two P atoms (P–P4–P bond angle = 118.8° with average P–P bond length =  $2.113 \pm 0.018$  Å). Slight deviations in both Na–P and P–P interatomic distances likely account for the deviations in CS tensors. In addition, the CS tensor of P2 NaP +112 meV above hull is also somewhat similar to that of the <sup>31</sup>P environment at  $\delta_{\text{iso}} = -78$  ppm, although the anisotropy is clearly smaller. The molecular fragment for P in NaP (+112 meV) is also a P helix, which is a disordered variant of the 4-fold P helix found in *c*-NaP. P2 in NaP (+112 meV) is also coordinated to five Na atoms (average Na–P interatomic distance =  $3.050 \pm 0.059$  Å) and two P atoms (P–P2–P bond angle = 109.5° with average P–P bond length =  $2.262 \pm 0.014$  Å). This structure is least likely to be representative of the P site for  $\delta_{\text{iso}} = -78$  ppm, which may be due to the deviation in P–P–P bond angles compared to those observed for larger anisotropies. Finally, the CSA at  $\delta_{\text{iso}} = -78$  ppm is also similar to that of P1 in Na<sub>2</sub>P found via GA +90 meV above the hull, which exhibits P–P dumbbells, although this structure shows the greatest deviation in asymmetry parameter. Therefore, we conclude that the P site at  $\delta_{\text{iso}} = -78$  ppm is best represented by a <sup>31</sup>P site that is part of a P helix, and is likely coordinated to five Na atoms and two P atoms.

The final <sup>31</sup>P site at  $\delta_{\text{iso}} = -143$  ppm closely resembles that of P4 in metastable NaP (+96 meV above the hull) found via GA (Figure 4d and Table 2). P4 in NaP (+96 meV) is coordinated to six Na (average Na–P interatomic distance =  $3.161 \pm 0.152$  Å) and one P (P–P bond length = 2.153 Å). Instead of P helices, this structure exhibits 4-member P zig-zags, with P4 serving as the terminal unit of the zig-zag motif. Furthermore, two other possible P motifs were identified from DFT, both of which exhibit different P motifs. First, the CS tensor of P6 NaP +94 meV above the hull found via GA shows reasonable agreement with the experimental CS tensor. This structure contains distorted 5-member P rings. P6 in NaP +94 meV (GA) is surrounded by is surrounded by five Na atoms (average Na–P interatomic distance =  $3.072 \pm 0.132$  Å) and two P atoms (P–P4–P bond angle = 118.4° with average P–P bond length =  $2.178 \pm 0.005$  Å). The CS tensor for P1 in

Na<sub>2</sub>P +91 meV above the hull, which contains P–P dumbbells is also similar to that of the <sup>31</sup>P site at  $\delta_{\text{iso}} = -143$  ppm. P1 Na<sub>2</sub>P above hull is coordinated to seven Na atoms (average Na–P interatomic distance =  $3.008 \pm 0.111$  Å) and one P atom (P–P bond length =  $2.401$  Å). Although the presence of additional structural motifs (e.g. rings and dumbbells) cannot be ruled out, neither motif agrees with the experimental CS tensor with the same accuracy of the terminal unit of four-member P zig-zags.

For NIBs charged to 0.80 V ( $4240 \text{ mA h g}^{-1}$ ), the <sup>31</sup>P species at  $\delta_{\text{iso}} = -29$  ppm shows good agreement with the P8 site of metastable Na<sub>7</sub>P<sub>8</sub> (+33 meV above the hull) found from GA (Figure 5a, Table 3). The P8 site is part of a P helical fragment and is bound to four Na atoms (average Na–P interatomic distance of  $3.123 \pm 0.203$  Å) and two P atoms, forming a P–P8–P bond angle =  $114.2^\circ$  (average P–P bond length =  $2.227 \pm 0.004$  Å). A somewhat similar CS tensor is observed for P1 Na<sub>5</sub>P<sub>6</sub> +84 meV above the hull, yet smaller anisotropy is noted. The P1 site in Na<sub>5</sub>P<sub>6</sub> (+84 meV) is also bound to four Na atoms (average Na–P interatomic distance of  $3.052 \pm 0.111$  Å) and two P atoms, forming a P–P8–P bond angle =  $98.6^\circ$  (average P–P bond length =  $2.212 \pm 0.003$  Å). While the anisotropy of the CS tensor is similar to that of P1 +91 meV above the hull, found via GA, the anisotropy does not match the experimental value (Table S1), indicating that this site is more likely to be part of a P helix than a 3-member P zig-zag.

The <sup>31</sup>P site at  $\delta_{\text{iso}} = -78$  ppm agrees well with the P1 environment found in metastable NaP (+89 meV above the hull) found via GA (Figure 5b, Table 3). The extended P structure in NaP (+89 meV) is again P helices. Like other P helices, the P1 site is coordinated to six Na atoms (average Na–P interatomic distance =  $3.097 \pm 0.133$  Å) and two P atoms (P–P1–P bond angle =  $113.5^\circ$  with an average P–P bond length of  $2.222 \pm 0.028$  Å). This site also shows a similar anisotropy to P1 in NaP +113 meV above the hull found from AIRSS, where P1 is present in a trigonal planar environment. Here, too much deviation is observed in the asymmetry parameter and this P motif likely does not represent the binding geometry.

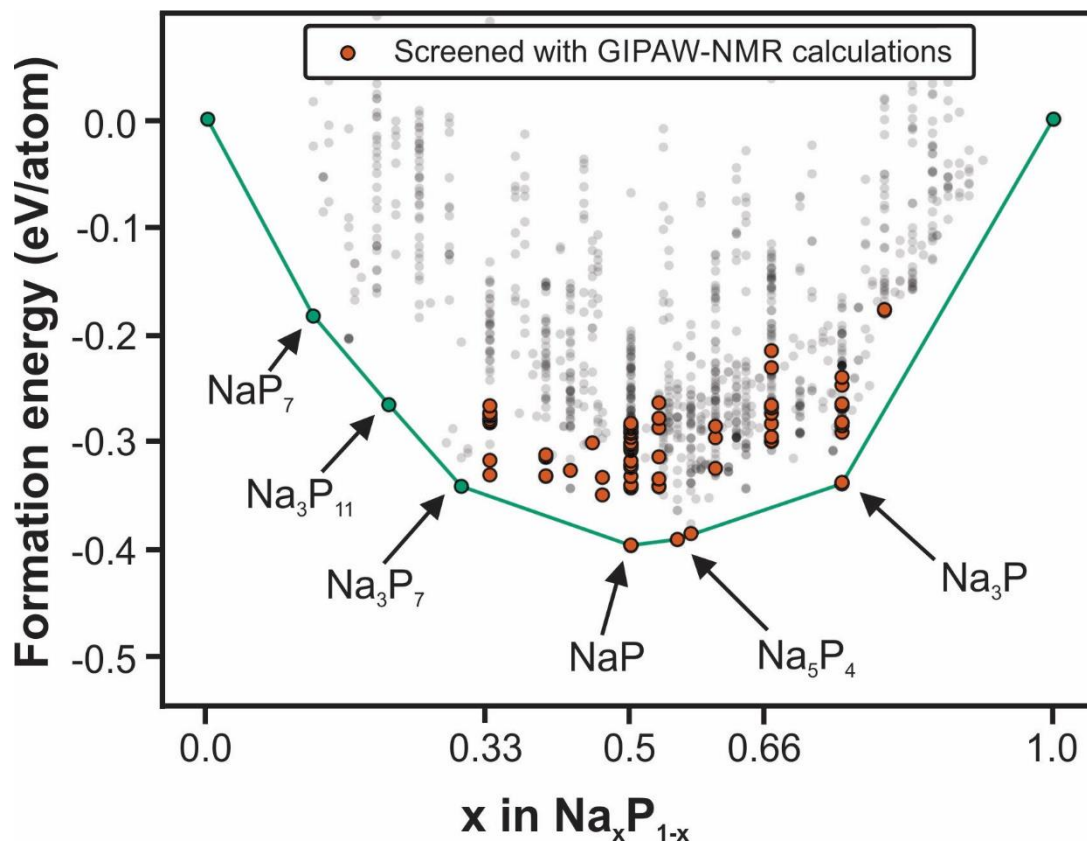


**Figure S12.** Convex hull of  $\text{Na}_x\text{P}_{1-x}$  predicted with DFT energies of known, AIRSS, or species-swapping derived phases from ref 38 (main text) and GA-derived phases depicted in Figure 1a of the main text. Orange circles represent structures that were screened with GIPAW-NMR calculations and green circles were screened with GIPAW-NMR in ref 38 (main text). NMR calculations were not performed on structures shown in gray.

### Powder X-ray diffraction.

*Ex situ* PXRD was collected for selected  $\text{Na}_x\text{P}$  intermediates for comparison to previous literature reports using both *ex* and *in situ* synchrotron high energy XRD<sup>12</sup> characterization of (de)sodiation in black P electrodes.

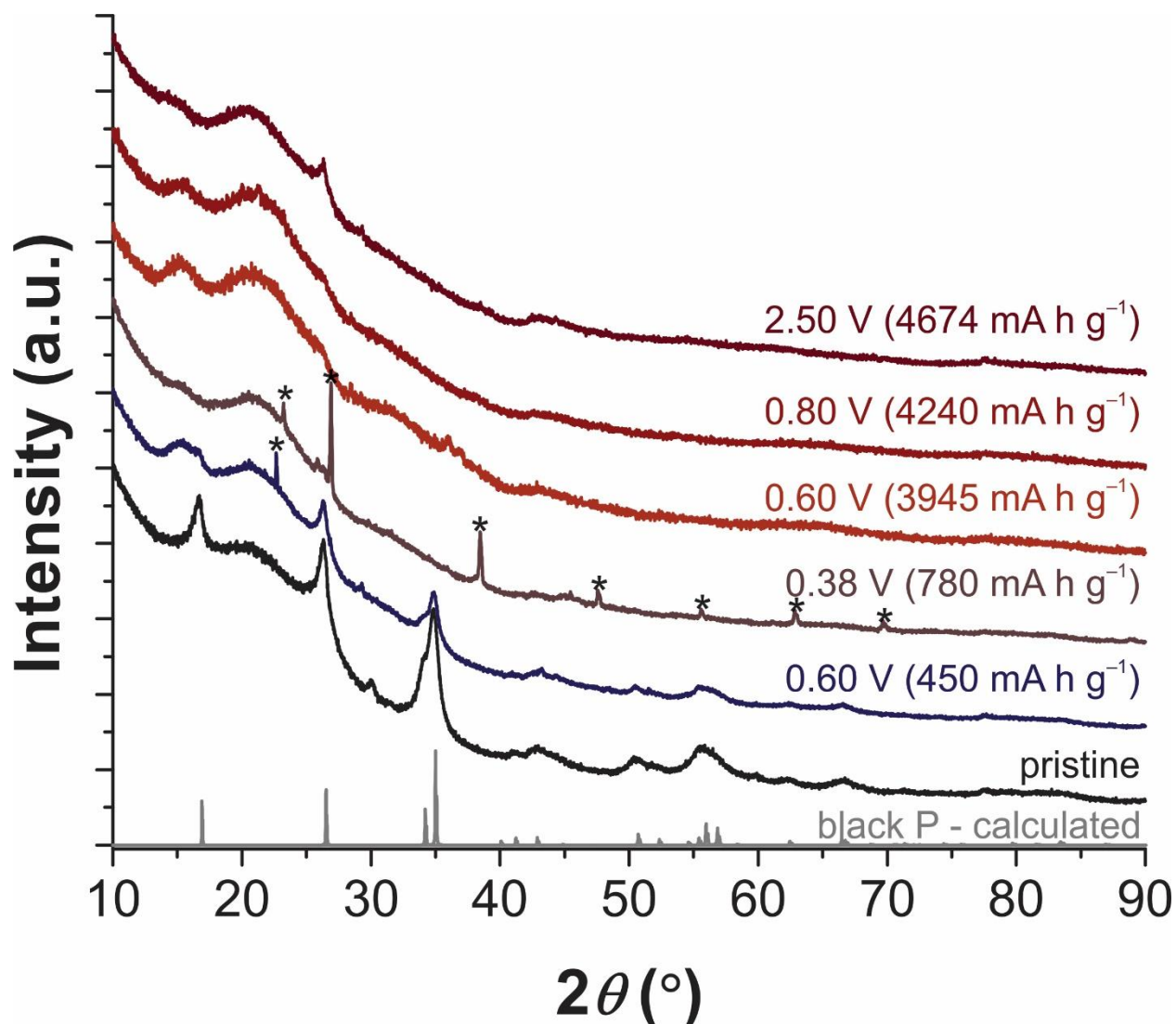


**Figure S13.** *Ex situ* PXRD patterns of  $\text{Na}_x\text{P}$  batteries collected at various stages of (de)sodiation, compared to the calculated pattern for black P (grey, bottom). Asterisks denote KBr contamination from the NMR rotors in the samples discharged (sodiated) to 0.60 V ( $450 \text{ mA h g}^{-1}$ ) and 0.38 V ( $780 \text{ mA h g}^{-1}$ ).

Bulk  $\text{Na}_3\text{P}$  was synthesized using a modified literature procedure for comparison to PXRD of the NIBs<sup>13</sup>. Briefly, metallic Na and red P powder were combined in a sealed Pyrex ampule, heated to 170 °C in 2 h, annealed for 30 min, heated to 350 °C in 5 h, annealed for 30 min, heated to 480 °C in 5 h, annealed for 5 h, and cooled to room temperature in 6 h.

**Table S2.** Coordinates and Wyckoff positions for the atoms in  $\text{Na}_3\text{P}-P6_3cm$  as refined from a sample derived by solid-state synthesis (cf. Figure S15). The displacement parameters of the atoms were fixed to  $U_{\text{iso}} = 0.013 \text{ pm}^2$ .

Atom	Wyckoff position	$x$	$y$	$z$
Na1	2a	0	0	0.259(2)
Na2	4b	1/3	2/3	0.2186(9)
Na3	6c	0.3195(7)	0	0.5886(6)
Na4	6c	0.3621(5)	0	-0.0725(6)
P	6c	0.336(1)	0	0.24588

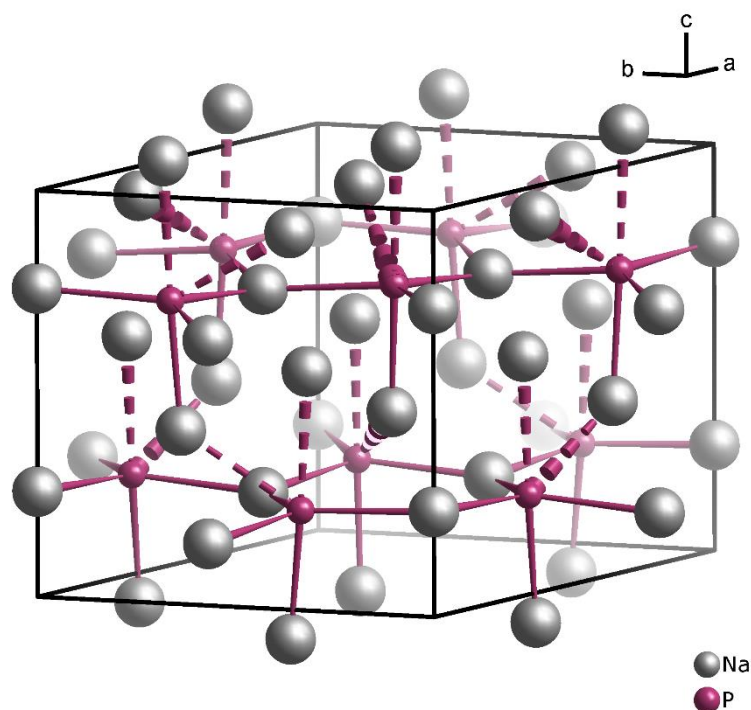


**Figure S14.** Crystal structure of  $\text{Na}_3\text{P}-P6_3cm$  derived from Rietveld refinement. Solid bonds indicate distances below 290 pm, dashed ones below 310 pm. Note the distortion and tilting of the  $\text{PNa}_5$  trigonal bipyramids as well as the capping of them by additional sodium atoms of adjacent bipyramids.

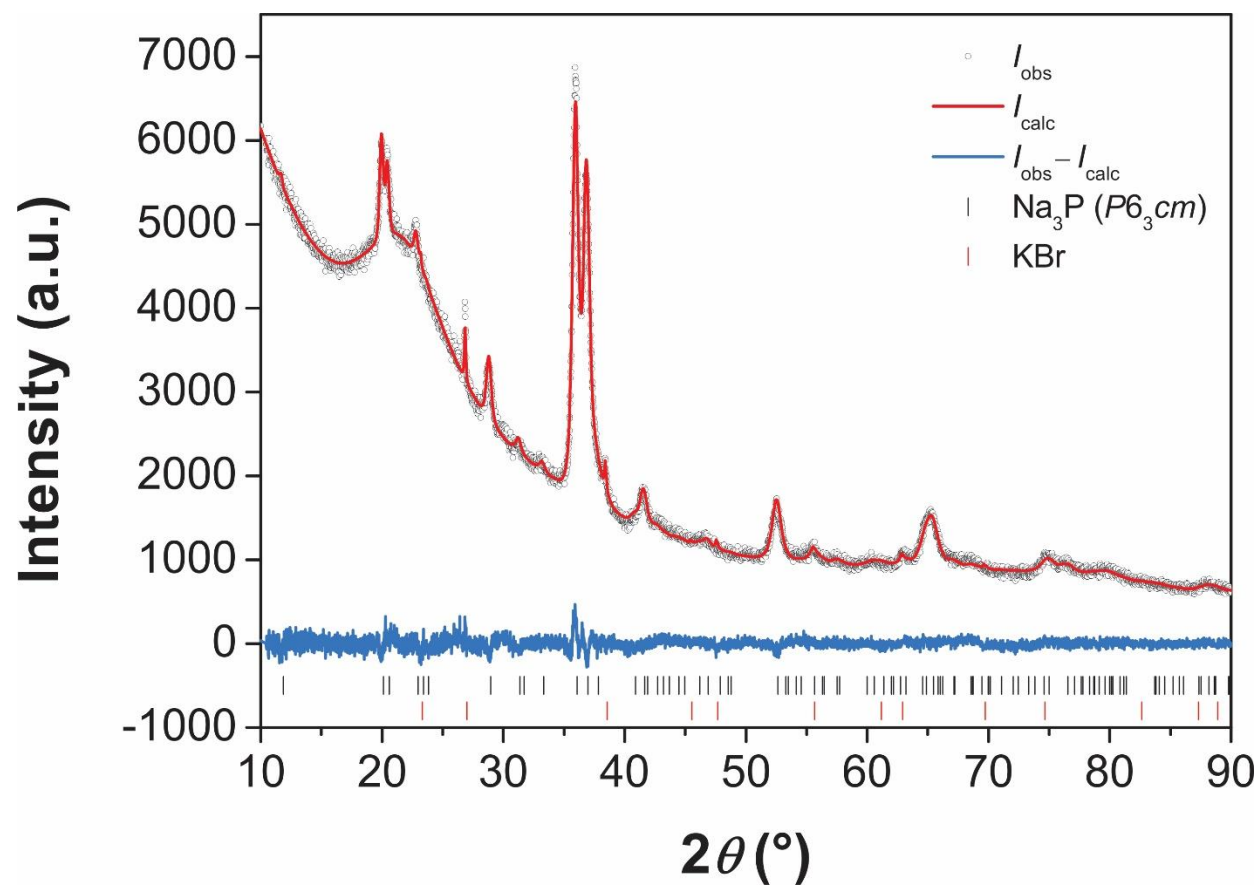


**Figure S15.** Rietveld refinement of a powder X-ray diffractogram (Cu- $K\alpha$  radiation;  $\lambda = 154.06$  pm, 154.43 pm) of a  $\text{Na}_3\text{P}$  sample in  $P6_3cm$  derived from discharging a battery to 0.01 V. KBr was used as internal standard.

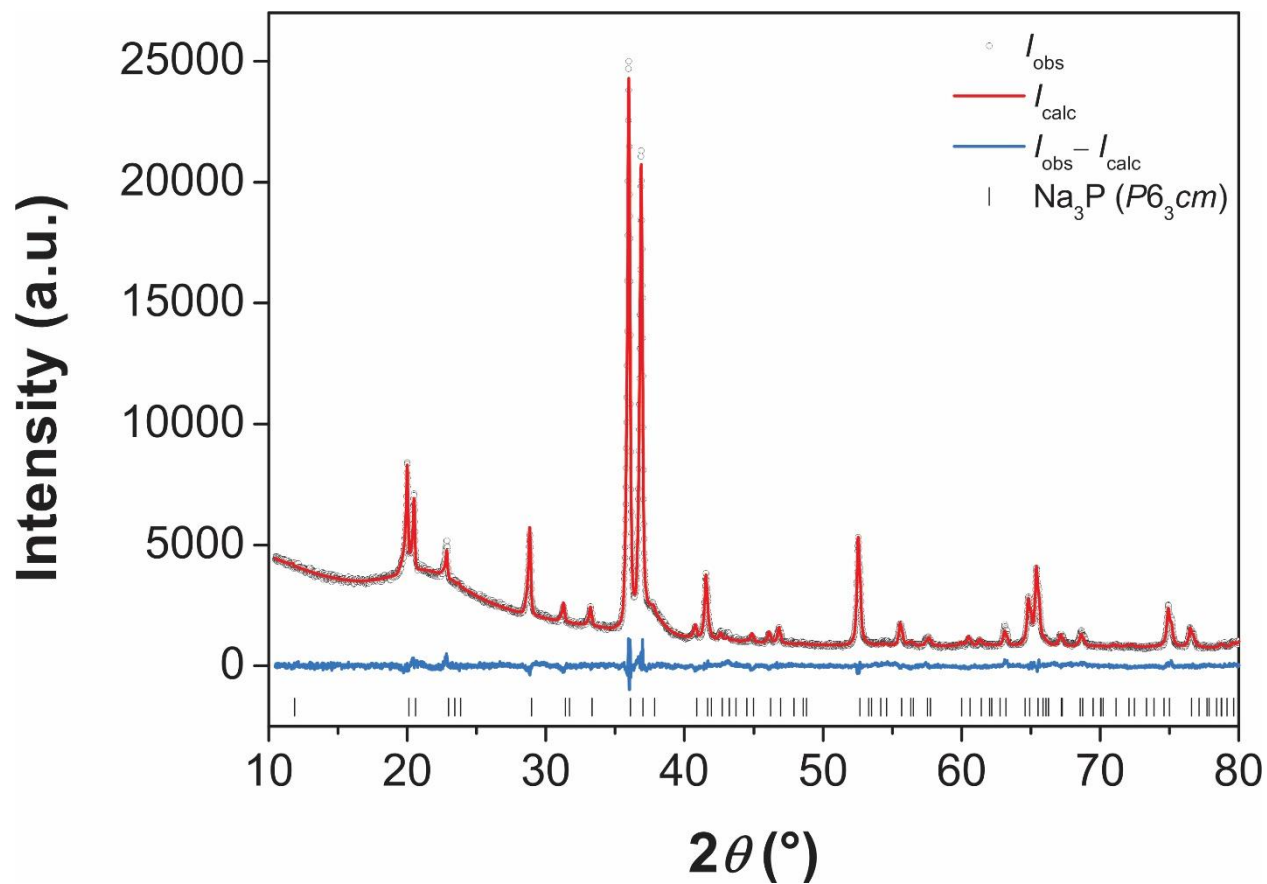


**Figure S16.** Rietveld refinement of a powder X-ray diffractogram (Cu- $K\alpha$  radiation;  $\lambda = 154.06$  pm,  $154.43$  pm) of a  $\text{Na}_3\text{P}$  sample in  $P6_3cm$  derived from a solid-state reaction of metallic Na and red P.

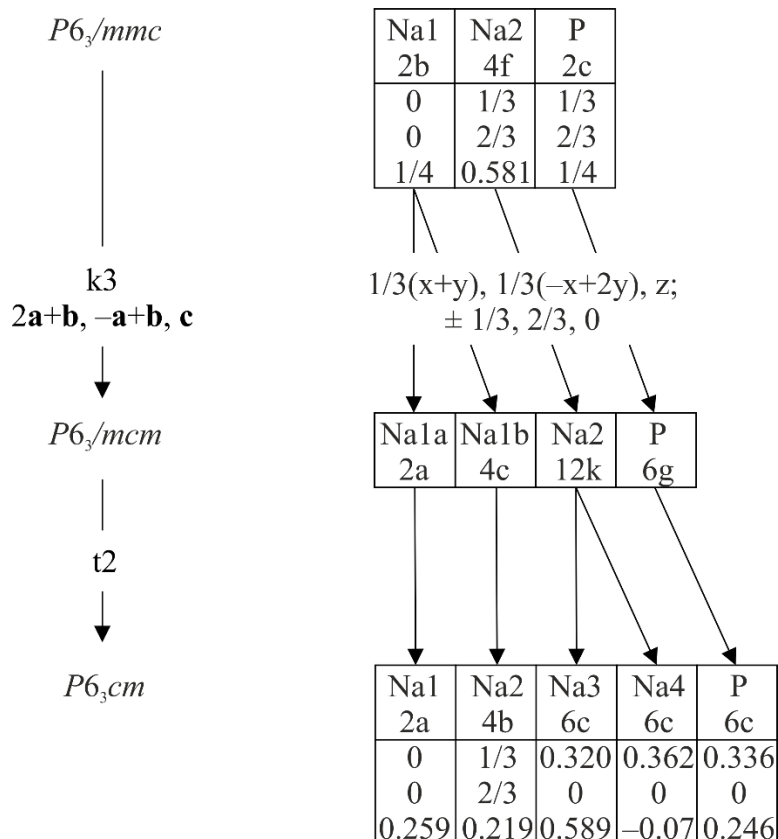


**Figure S17.** Bärnighausen tree for the symmetry relationship between the two  $\text{Na}_3\text{P}$  structure models in  $P6_3cm$  and  $P6_3/mmc$  (via  $P6_3/mcm$ ).

## References

1. Wasylishen, R. E.; Ashbrook, S. E.; Wimperis, S., *NMR of quadrupolar nuclei in solid materials*. John Wiley & Sons: West Sussex, 2012.
2. Gan, Z., *J. Am. Chem. Soc.* **1992**, *114*, 8307.
3. Antzutkin, O. N.; Shekar, S. C.; Levitt, M. H., *J. Magn. Reson. A* **1995**, *115*, 7.
4. Dixon, W. T., *J. Chem. Phys.* **1982**, *77*, 1800.
5. Clément, R. J.; Pell, A. J.; Middlemiss, D. S.; Strobridge, F. C.; Miller, J. K.; Whittingham, M. S.; Emsley, L.; Grey, C. P.; Pintacuda, G., *J. Am. Chem. Soc.* **2012**, *134*, 17178.
6. Hung, I.; Zhou, L.; Pourpoint, F.; Grey, C. P.; Gan, Z., *J. Am. Chem. Soc.* **2012**, *134*, 1898.
7. Liu, H.; Bugnet, M.; Tessaro, M. Z.; Harris, K. J.; Dunham, M. J. R.; Jiang, M.; Goward, G. R.; Botton, G. A., *Phys. Chem. Chem. Phys.* **2016**, *18*, 29064.
8. Strobridge, F. C.; Middlemiss, D. S.; Pell, A. J.; Leskes, M.; Clement, R. J.; Pourpoint, F.; Lu, Z.; Hanna, J. V.; Pintacuda, G.; Emsley, L.; Samoson, A.; Grey, C. P., *J. Mater. Chem. A* **2014**, *2*, 11948.
9. Xu, J.; Lee, D. H.; Clément, R. J.; Yu, X.; Leskes, M.; Pell, A. J.; Pintacuda, G.; Yang, X.-Q.; Grey, C. P.; Meng, Y. S., *Chem. Mater.* **2014**, *26*, 1260.

10. Zheng, S.; Zhong, G.; McDonald, M. J.; Gong, Z.; Liu, R.; Wen, W.; Yang, C.; Yang, Y., *J. Mater. Chem. A* **2016**, *4*, 9054.
11. Duer, M. J., *Solid state NMR spectroscopy: principles and applications*. John Wiley & Sons: Oxford, 2002.
12. Xu, G.-L.; Chen, Z.; Zhong, G.-M.; Liu, Y.; Yang, Y.; Ma, T.; Ren, Y.; Zuo, X.; Wu, X.-H.; Zhang, X.; Amine, K., *Nano Lett.* **2016**, *16*, 3955.
13. Jarvis, R. F.; Jacubinas, R. M.; Kaner, R. B., *Inorg. Chem.* **2000**, *39*, 3243.